Coupling of Navier–Stokes equations with protein molecular dynamics and its application to hemodynamics‡

Yaling Liu[1], Lucy Zhang[2], Xiaodong Wang[3] and Wing Kam Liu[1,*,†]

[1]*Department of Mechanical Engineering, 2145 Sheridan Road, Northwestern University, Evanston, IL 60208, U.S.A.*
[2]*Department of Mechanical Engineering, 6823 Saint Charles Avenue, Tulane University, New Orleans, LA 70118, U.S.A.*
[3]*Department of Mathematical Sciences, University Heights, Newark, NJ 07102, U.S.A.*

SUMMARY

The red blood cell (RBC) aggregation plays an important role in many physiological phenomena, in particular the atherosclerosis and thrombotic processes. In this research, we introduce a new modelling technique that couples Navier–Stokes equations with protein molecular dynamics to investigate the behaviours of RBC aggregates and their effects on the blood rheology. In essence, the Lagrangian solid mesh, which represents the immersed deformable cells, is set to move on top of a background Eulerian mesh. The effects of cell–cell interaction (adhesive/repulsive) and hydrodynamic forces on RBC aggregates are studied by introducing equivalent protein molecular potentials into the immersed finite element method. The aggregation of red blood cells in quiescent fluids is simulated. The de-aggregation of a RBC cluster at different shear rates is also investigated to provide an explanation of the shear-rate-dependence of the blood viscoelastic properties. Finally, the influences of cell–cell interaction, RBC rigidity, and vessel geometry are addressed in a series of test cases with deformable cells (normal and sickle RBCs) passing through micro- and capillary vessels. Copyright © 2004 John Wiley & Sons, Ltd.

KEY WORDS: Immersed Finite Element Method; Reproducing Kernel Particle Method; fluid–structure interaction; Navier–Stokes equations; protein molecular dynamics; red blood cell; aggregation; coagulation; microcirculation; capillary

1. INTRODUCTION

Human blood circulatory systems have evolved to supply nutrients and oxygen to, and carry the waste away from, the cells of multi-cellular organisms through the transport of blood,

---

*Correspondence to: W. K. Liu, Department of Mechanical Engineering, 2145 Sheridan Road, Northwestern University, Evanston, IL 60208, U.S.A.
†E-mail: w-liu@northwestern.edu

a complex fluid composed of deformable cells, proteins, platelets, and plasma. Currently, cardiovascular diseases represent the leading cause of death in developed countries. The lack of understanding of short and long-term development and evolution of many of the arterial and vascular diseases directly limits the disease diagnosis and prevention as well as the planning of the therapeutic approaches. It is therefore of significant clinical relevance to understand blood composition and its rheological behaviours in the context of multi-scale and multi-physics hemodynamics.

As depicted in Fahraeus–Lindqvist effects, blood viscosity is lower in small vessels than in large vessels. In fact, the viscosity in capillaries is less than half of that in large vessels in part due to red cells moving together in single files through small vessels. While theories of suspension rheology generally focus on homogeneous flows in infinite domains, the important phenomena of blood flows in micro-circulation depend on the combined effects of vessel geometries, cell deformability, wall compliance, flow shear rates, and many micro-scale chemical, physiological, and biological factors [1, 2]. There have been past studies on shear flow effects on one or two cells [3], leukocytes adhesion to vascular endothelium [4], and particulate flow based on continuum enrichment methods [5, 6]. However, no mature theory is yet available for the prediction of blood rheology and blood perfusion through micro-vessels and capillary networks. The different time and length scales as well as large motions and deformations of immersed solids pose tremendous challenges to the mathematical modelling of blood flow at that level [7, 8].

In this paper, we concentrate on the rheological aspects of flow systems of arterioles, capillaries, and venules which involve deformable cells, cell–cell interactions, and compliant vessels. In particular, we propose a new modelling technique with a combination of the newly developed immersed finite element method (IFEM) [9] and protein molecular dynamics.

We first give a detailed description of the discrete red blood cell (RBC) and aggregation models in Section 2. In Section 3, we illustrate the key ingredients of the proposed combination of the IFEM and protein molecular dynamics. The discussion and conclusions of the RBC aggregation test models are presented in Sections 4 and 5.

2. MATHEMATICAL MODELS

2.1. Discrete RBC model

The role of RBCs in the human body is to pick up oxygen as the blood passes through the lungs and release it to the cells over the entire body. The RBC membrane contains a lipid bilayer structure. Unlike the white blood cell, in suspension culture, RBC assumes a biconcave disc shape which permits its passage through capillaries. The biconcave disc shape enables the surface-to-volume ratio of a typical RBC to be significantly higher than that of a sphere formed by a tensioned membrane.

As shown in Figure 1, to account for both bending and membrane rigidities, RBC membrane is modelled with a three-dimensional finite element formulation using the Lagrangian description. Thus, a RBC is modelled as a flexible three-dimensional thin structure enclosing an incompressible fluid. In this work, a typical membrane is discretized with 1043 nodes and 4567 tetrahedra elements. Moreover, a function is used to describe the x–y co-ordinates of the
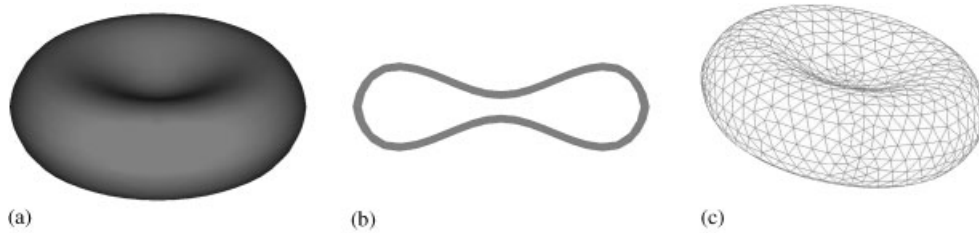
Figure 1. A three-dimensional finite element mesh of a single RBC model:
(a) 3D RBC model; (b) RBC cross-section; (c) RBC mesh.

cross-sectional profile [10]:

$$\bar{y} = 0.5[1 - \bar{x}^2]^{1/2}(a_0 + a_1\bar{x}^2 + a_2\bar{x}^4), \quad -1 \leqslant \bar{x} \leqslant 1 \tag{1}$$

with $a_0 = 0.207$, $a_1 = 2.002$, and $a_2 = 1.122$, and the non-dimensional co-ordinates $\bar{x}$ and $\bar{y}$ are scaled as $x/5$ and $y/5\ \mu$m, respectively.

Finally, a Neo-Hookean strain energy function is used to depict the material behaviour of the RBC membrane:

$$W = C_1(J_1 - 3) + \frac{C_2}{2}(J_2 - 1)^2 \tag{2}$$

with the material properties C_1 and C_2, where J_1 and J_2 are the functions of the invariants of the deformation gradient $\mathbf{C}$ as defined in References [9, 11].

2.2. RBC aggregation

Cell–cell adhesion plays an important role in various physiological phenomena including the recognition of foreign cells [12]. Although the exact physiological mechanisms of the RBC coagulation and aggregation are still ambiguous, it has been found that both the RBC surface structure and membrane proteins are key factors in producing adhesive/repulsive forces. The proposed explanations in general fall into two categories: the bridging and adsorption models with the adsorption and exclusion of the plasmatic macromolecules at RBC surfaces, respectively. The primary macromolecules that cause the RBC aggregation are the so-called fibrinogen. The depletion layer results in a reduction of osmotic pressure in the gap between nearby RBCs, which consequently produces an attractive force. It can be assumed that the adhesion between RBCs will occur only if the RBCs are close enough. Nevertheless, when the nearby RBCs are too close to each other, a repulsive force will hinder them from contact. The repulsive forces include the steric forces due to the glycocalyx and the electrostatic repulsive force induced from the same negative fixed charges at RBC surfaces. Of course, the level of the RBC aggregation depends on the initial position of the cells and the strength of the adhesive force in comparison with other forces, such as hydrodynamic forces.

The aim of this paper is not to identify the exact mechanism of the RBC coagulation and aggregation. Instead, we focus on the study of the behaviours of RBC aggregates and their effects on viscoelastic properties of blood flows. To our knowledge, it is the first attempt to study this phenomenon using three-dimensional continuum models of the RBC aggregation
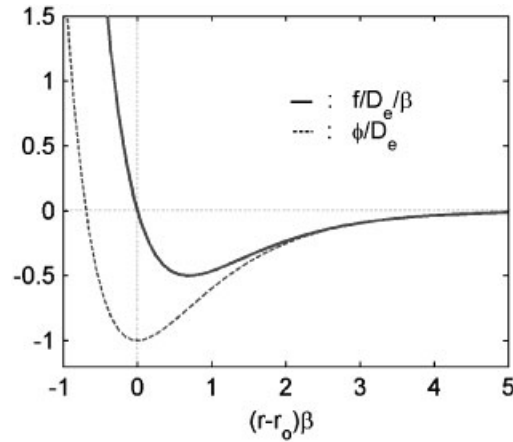
Figure 2. Non-dimensionalized Morse potential and force.

with the effects of shear rates, RBC geometries, cell–cell interaction forces, and non-linear material descriptions.

Recently, Neu and Meiselman [13] proposed a theoretical model for depletion-mediated RBC aggregation in polymer solutions. The basic behaviour of the interaction forces between two RBCs is simply illustrated as the weak attractive and strong repulsive forces at far and near distances. Due to the complexity of the aggregation process, we accumulate the intermolecular force, electrostatic force, and protein dynamics into a potential function, similar to an intermolecular potential. Here we adopt the Morse potential, found to be capable of generating similar interactional energy versus RBC–RBC separation distance plot given in Reference [13]. As shall be seen later, the aggregation behaviours simulated by this potential qualitatively agree with experimental observations:

$$\phi(r) = D_e[e^{2\beta(r_0-r)} - 2e^{\beta(r_0-r)}] \tag{3}$$

$$f(r) = -\frac{\partial \phi(r)}{\partial r} = 2D_e\beta[e^{2\beta(r_0-r)} - e^{\beta(r_0-r)}] \tag{4}$$

where r_0 and D_e stand for the zero force length and surface energy, respectively, and β is a scaling factor. The non-dimensionalized Morse potential and force are plotted in Figure 2.

2.3. Blood viscoelasticity

Blood plasma can be accurately modelled with the Newtonian fluid model, yet blood flows do exhibit non-Newtonian or viscoelastic behaviours, particularly under low Reynolds numbers. In fact, human blood is a typical thixotropic material of which the viscoelastic characteristics may vary significantly with its stress and strain levels. In practice, we often characterize the blood flow with the strength of the shear flow which is measured with the shear rate $\dot{\gamma}$ within the range from 0.1 to $100\,\text{s}^{-1}$.

An illustration of the shear-rate-dependence of blood viscoelasticity is shown in Figure 3. It is clear that as the shear rate increases the blood viscosity decreases initially and even-
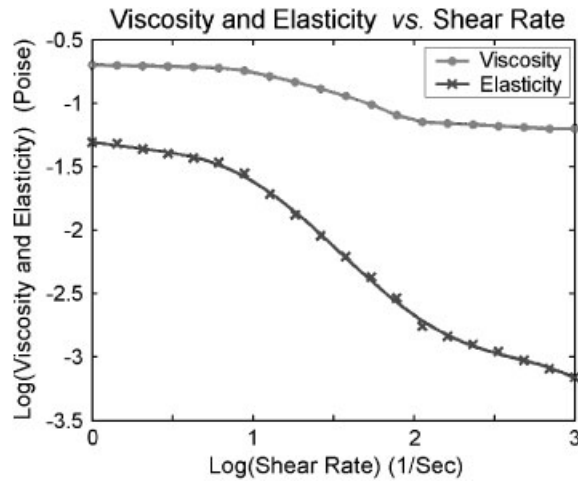
Figure 3. An illustration of the shear-rate-dependence of blood viscoelasticity (reproduced based on http://www.vilastic.com/TECH10.html).
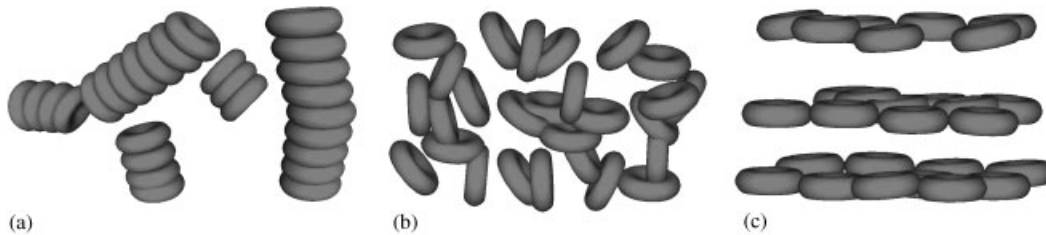

Figure 4. Blood microscopic changes under different shear rates: (a) Low shear region; (b) mid-shear region; (c) high shear region.

tually reaches a plateau marking the plasma viscosity, and the blood elasticity continues to decrease.

On the microscopic level, RBCs play an important role in the blood viscoelastic behaviours [14, 15]. In the quiescent state, normal RBCs tend to aggregate. Under low shear rate, aggregates are mainly influenced by the cell–cell interaction forces; in the mid-shear rate region, RBC aggregates start to disintegrate and the influence of the deformability gradually increases; and under high shear rate, RBCs tend to stretch, align with the flow, and form layers. The illustration of these three different stages is shown in Figure 4.

3. IFEM WITH PROTEIN MOLECULAR DYNAMICS

Let us consider an incompressible three-dimensional deformable structure in Ω^s (i.e. RBC membranes) completely immersed in an incompressible fluid domain Ω^f. The boundary of the deformable structure is denoted as Γ^s. Together, the fluid and the solid occupy a domain

Ω, but they do not intersect:

$$\Omega^f \cup \Omega^s = \Omega \quad \text{and} \quad \Omega^f \cap \Omega^s = \emptyset \tag{5}$$

In this work, we have extended the pioneer work of Professor Charles Peskin and co-workers on the Immersed Boundary (IB) method [16] to the so called Immersed Finite Element Method (IFEM) [11]. In contrast to the IB formulation, the solid domain can occupy a finite volume in the fluid domain. Since we assume both the fluid and the solid to be incompressible, the union of two domains can be treated as one incompressible continuum with a continuous velocity field. In the computation, the fluid spans over the entire domain Ω, thus an Eulerian fluid mesh is adopted; whereas a Lagrangian solid mesh is constructed on top of the Eulerian fluid mesh.

In the computational fluid domain Ω, the fluid grid is represented by the time-invariant position vector $\mathbf{x}$; while the material points of the structure in the initial solid domain Ω_0^s and the current solid domain Ω^s are represented by $\mathbf{X}^s$ and $\mathbf{x}^s(\mathbf{X}^s, t)$, respectively. The superscript s is used in the solid variables to distinguish the fluid and solid domains.

In the fluid calculations, the velocity $\mathbf{v}$ and the pressure p are the unknown fluid field variables; whereas the solid domain involves the calculation of the nodal displacement $\mathbf{u}^s$, which is defined as the difference of the current and the initial co-ordinates: $\mathbf{u}^s = \mathbf{x}^s - \mathbf{X}^s$.

To delineate the Lagrangian description for the solid and the Eulerian description for the fluid, we introduce different velocity field variables v_i^s and v_i to represent the motions of the solid in the domain Ω^s and the fluid within the entire domain Ω. The coupling of both velocity fields is accomplished with the Dirac delta function:

$$v_i^s(\mathbf{X}^s, t) = \int_\Omega v_i(\mathbf{x}, t)\, \delta(\mathbf{x} - \mathbf{x}^s(\mathbf{X}^s, t))\, \mathrm{d}\Omega \tag{6}$$

As illustrated in details in References [9, 11], we define the fluid–structure interaction force within the domain Ω^s as $f_i^{\mathrm{FSI},s}$, where FSI stands for fluid–structure interaction:

$$f_i^{\mathrm{FSI},s} = -(\rho^s - \rho^f)\frac{\mathrm{d}v_i}{\mathrm{d}t} + \sigma_{ij,j}^s - \sigma_{ij,j}^f + (\rho^s - \rho^f)g_i \quad \text{in } \Omega^s \tag{7}$$

The fluid–structure interaction force $f_i^{\mathrm{FSI},s}$ within the domain Ω^s can be illustrated as the force exerted on the surrounding fluid from the immersed solid.

The cell–cell interaction force is applied on the surfaces of cells:

$$\sigma_{ij}^s n_j = f_i^c \tag{8}$$

The transformation of the weak form from the updated Lagrangian to the total Lagrangian description is to change the integration domain from Ω^s to Ω_0^s. Since we consider incompressible fluid and solid, in the solid domain, the Jacobian determinant is 1, and the transformation of the weak form to total Lagrangian description yields

$$\int_{\Omega_0^s} \delta u_i(\rho^s - \rho^f)\ddot{u}_i^s\, \mathrm{d}\Omega_0^s + \int_{\Omega_0^s} \delta u_{i,j} P_{ji}\, \mathrm{d}\Omega_0^s - \int_{\Gamma_0^s} \delta u_i f_i^c\, \mathrm{d}\Gamma_0^s$$
$$- \int_{\Omega_0^s} \delta u_i(\rho^s - \rho^f)g_i\, \mathrm{d}\Omega_0^s + \int_{\Omega_0^s} \delta u_i f_i^{\mathrm{FSI},s}\, \mathrm{d}\Omega_0^s = 0 \tag{9}$$
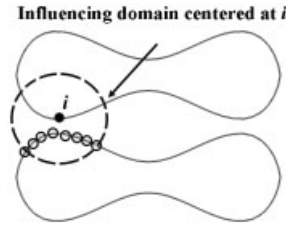
Figure 5. Illustration of an influencing domain of surface interaction within a cut-off radius.

where the first Piola–Kirchhoff stress P_{ij} is defined as $P_{ij} = JF_{ik}^{-1}\sigma_{kj}^s$ and the deformation gradient F_{ij} as $F_{ij} = \partial x_i / \partial X_j$.

For structures with large displacements and deformations, the second Piola–Kirchhoff stress S_{ij} and the Green–Lagrangian strain E_{ij} are used in the total Lagrangian formulation:

$$S_{ij} = \frac{\partial W}{\partial E_{ij}} \quad \text{and} \quad E_{ij} = \frac{1}{2}(C_{ij} - \delta_{ij}) \tag{10}$$

where the first Piola–Kirchhoff stress P_{ij} can be obtained from the second Piola–Kirchhoff stress as $P_{ij} = S_{ik}F_{jk}$.

With respect to the cell–cell interaction force, as shown in Figure 2, the cut-off length is chosen to be around $3\,\mu m$, beyond which the attractive force decays very fast, i.e. the nodes that are outside of the influencing domain, essentially a sphere with the cut-off length as its radius, have very little effects. Moreover, the potential function is chosen such that the RBCs will de-aggregate at the shear rate above $0.5\,s^{-1}$, according to the experimental observation [17]. In this paper, for convenience, we set the zero force length as 250 nm. However, as we reduce the zero force length, local enrichment and multi-scale coupling must also be introduced. This topic will be addressed separately in a different paper.

In the actual implementation, after the finite element discretization of the solid domain, as depicted in Figure 5, a sphere with the diameter of the cut-off length is used to identify the cell surface $\mathbf{Y}^c$ within the influencing domain around the cell surface $\mathbf{X}^c$. Hence, a typical cell–cell interaction force can be denoted as:

$$\mathbf{f}^c(\mathbf{X}^c) = -\int_{\Gamma(\mathbf{Y}^c)} \frac{\partial \phi(r)}{\partial r}\frac{\mathbf{r}}{r}\,d\Gamma \tag{11}$$

where $\mathbf{r} = \mathbf{X}^c - \mathbf{Y}^c$, $r = \|\mathbf{X}^c - \mathbf{Y}^c\|$, and $\Gamma(\mathbf{Y}^c)$ represents cell surface area within the influencing domain surrounding surface $\mathbf{X}^c$.

In actuality, $\mathbf{f}^c$ represents the cell–cell interaction force at a surface point exerted by the surfaces of other cells nearby, which is defined as the force per unit area. Naturally, the interaction force $f_i^{\mathrm{FSI},s}$ in Equation (7) is calculated with the Lagrangian description. Moreover, a Dirac delta function δ is used to distribute the interaction force from the solid domain onto the computational fluid domain Ω:

$$f_i^{\mathrm{FSI}}(\mathbf{x},t) = \int_{\Omega^s} f_i^{\mathrm{FSI},s}(\mathbf{X}^s,t)\,\delta(\mathbf{x} - \mathbf{x}^s(\mathbf{X}^s,t))\,d\Omega \tag{12}$$

Hence, the equivalent governing equation for the fluid is derived by combining the fluid terms and the interaction force as:

$$\rho^f \frac{\mathrm{d}v_i}{\mathrm{d}t} = \sigma^f_{ij,j} + f^{\mathrm{FSI}}_i \quad \text{in } \Omega \tag{13}$$

Since we consider the entire domain Ω to be incompressible, we only need to apply the incompressibility constraint once in the entire domain Ω:

$$v_{i,i} = 0 \tag{14}$$

The non-linear systems (13) and (14) are solved with the standard stabilized Galerkin method and the Newton–Raphson iteration [18, 19]. Moreover, to improve the computation efficiency, we also employ the GMRES iterative algorithm and compute the residuals based on matrix-free techniques [20, 21].

Finally, in the interpolation process from the fluid onto the solid grid, the discretized form of Equation (6) can be written as

$$v^s_{iI} = \sum_J v_{iJ}(t)\phi_J(\mathbf{x}_J - \mathbf{x}^s_I), \quad \mathbf{x}_J \in \Omega_{\phi I} \tag{15}$$

where the discretized delta function ϕ_J is the kernel function introduced in the reproduced kernel particle method (RKPM) [22].

Here, the solid velocity $\mathbf{v}^s_I$ at node I can be calculated by gathering the velocities at fluid nodes within the influence domain $\Omega_{\phi I}$. A dual procedure takes place in the distribution process from the solid onto the fluid grid. The discretized form of Equation (12) is expressed as

$$f^{\mathrm{FSI}}_{iJ} = \sum_I f^{\mathrm{FSI},s}_{iI}(\mathbf{X}^s, t)\phi_I(\mathbf{x}_J - \mathbf{x}^s_I), \quad \mathbf{x}^s_I \in \Omega_{\phi J} \tag{16}$$

By interpolating the fluid velocities onto the solid particles in Equation (15), the fluid within the solid domain is bounded to solid material points. This ensures not only the no-slip boundary condition on the surface of the solid, but also automatically stops the fluid from penetrating the solid, provided the solid mesh is at least two times denser than the surrounding fluid mesh. This heuristic criterion is based on the numerical evidence and needs further investigation.

4. APPLICATIONS TO HEMODYNAMICS

One microliter of normal human blood contains about 5 000 000 RBCs, 7000 white blood cells, and 300 000 platelets. At this point, even with the current multi-physics and multi-scale computational tools, it is still impossible to handle such complex fluids as a whole. In this paper, we focus on a three-dimensional Newtonian fluid interacting with a few flexible RBCs. To illustrate clearly the deformation of the RBCs, two-dimensional cross-sections of the membranes are shown in some examples in this section.

RBCs, or erythrocytes are normally 8–10 μm in diameter and 7.5–10 nm in thickness. The RBC density is approximately 15% higher than that of the water. The RBC membrane has a shear modulus of 4.2×10^{-3} dyn/cm^2, a dilation modulus of 500 dyn/cm^2, and a bending modulus of 1.8×10^{-12} dyn/cm^2. Since the shear modulus of the RBC membrane is much

smaller than the dilation modulus, the RBC membrane is susceptible to deformation by shear with very little area change. Moreover, the inner cytoplasm is assumed to be an incompressible Newtonian fluid with the same viscosity as the plasma, i.e. 0.01 dyn s/cm^2.

The mechanical properties and functions of blood flows are strongly influenced by complex multi-scale and multi-physics factors, three of which, namely cell–cell interaction forces, shear rates, and vessel geometries will be examined with the proposed numerical procedures.

4.1. Cell–cell interaction and shear rate effects

RBC aggregation is one of the main causes of the non-Newtonian behaviours of blood flows. Due to the presence of the cross-linking proteins fibrinogen on cell membranes and globulin in the plasma, RBCs tend to form aggregates called rouleaus, in which RBCs adhere loosely like a stack of coins. The presence of massive rouleaus can impair the blood flow through micro- and capillary vessels and cause fatigue and shortness of breath. The variation in the level of RBC aggregation may be an indication of the thrombotic disease.

In general, the cell–cell interaction forces are not sufficient to deform cell membranes. However, the ensuing aggregate could alter the surrounding fluid significantly. To illustrate the aggregation formation, we consider two RBCs attracting each other in the quiescent fluid. In order to show clearly the effects of cell–cell interaction forces, we enlarge the magnitude of the interaction force by five times. As shown in Figure 6, under strong cell–cell interaction forces, two disassociated cells gradually move together and form a doublet with moderate deformations.

To study the effects of cell–cell interaction on RBC aggregates, we introduce a four-RBC model with and without cell–cell interaction forces under different shear rates. The four-RBC model is placed at the centre of the fluid domain with vertical centre distance of 3.96 μm. Due to the biconcave shape, the adhesive/repulsive forces mainly exist around the perimeters of RBCs as shown in Figures 5 and 7.

With the boundary shear velocity of 5 μm/s for both upper and bottom surfaces, we get a shear rate of 0.5 s^{-1}. In Figure 7, the four-RBC model is subjected to three different shear

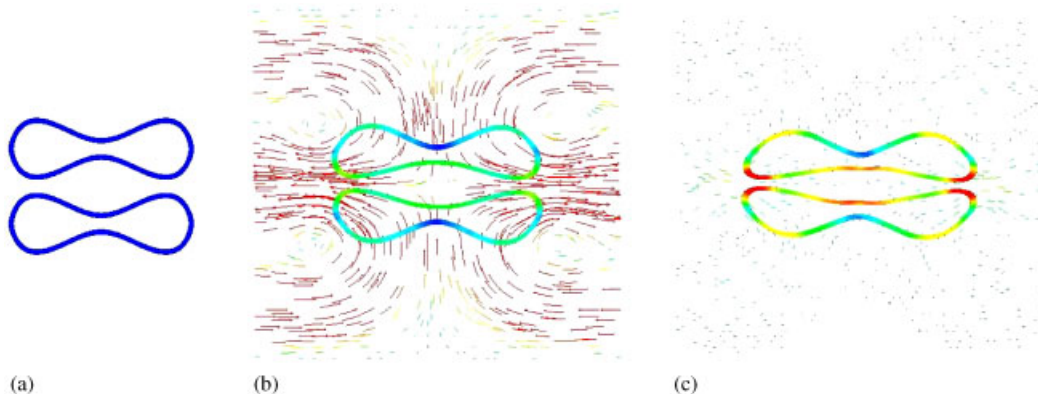(a)   (b)   (c)

Figure 6. Illustrations of the initial configuration of the two-RBC model and the deformation in the quiescent fluid under the influence of cell–cell interaction forces.
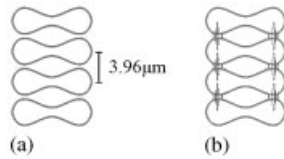
Figure 7. Illustrations of the initial configuration of the four-RBC model and cell–cell interaction forces.
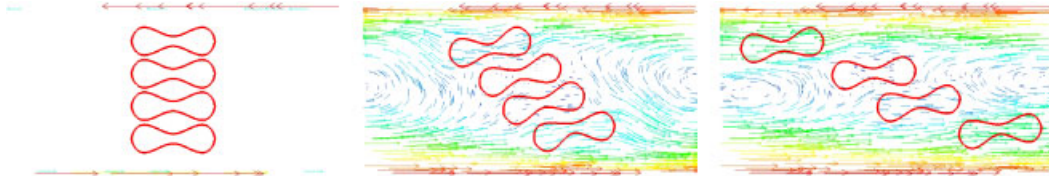

Figure 8. The shear of the four-RBC model at the shear rate of $0.25\,\mathrm{s}^{-1}$ without cell–cell interaction forces, at $t = 0$, 2, and 4 s. The vortexes are also shown in the figure.

rates. As expected, without cell–cell interaction forces, the RBCs will rotate and align with the flow separately while maintaining their vertical separations as shown in Figure 8. On the other hand, the RBC aggregate with cell–cell interaction forces rotates initially as a bulk with varying vertical distances. The comparison shows that cell–cell interaction forces restrain the disintegration of RBC aggregates and introduce elasticity in the blood's macroscopic mechanical behaviour.

In a set of numerical experiments, we subject the RBC aggregate and viscous fluid mixer to low shear rates and observe that RBC aggregate rotates as a bulk, as shown in Figure 9. With an intermediate shear rate, our numerical simulation demonstrates that after the initial rotations the RBC aggregate aligns with the shear direction and then de-aggregates as shown in Figure 10. At higher shear rate, the RBC aggregate completely disintegrates and the cells begin to orient themselves into parallel layers as shown in Figure 11. The disintegration of RBC aggregates with the increase of the shear rate is an indication of the decrease of the macroscopic viscosity, which is consistent with the experimental observation.

In another experiment with a multiple-cell aggregate blocking the flow, a high shear rate induces the RBC aggregate to rotate first and then partially disintegrate and eventually align the cells into parallel layers of RBCs as shown in Figure 12. As the evidence of excellent numerical resolution of the proposed combination of the IFEM and protein molecular dynamics, the fluid vorticities surrounding the deformable cells are clearly captured along with the large structural motions and deformations.

4.2. Micro- and capillary vessels

RBCs are important for blood flows in microcirculation. The typical diameter of the micro-vessel is 1.5–3 times larger than that of the cell. On the other hand, the capillary vessel diameter is about 2–4 μm which is significantly smaller. The pressure gradient which drives the flow is usually around 3.2–3.5 kPa. For the chosen diameter and pressure, the Reynolds number in a typical capillary is around 0.01. In fact, in the process of squeezing through
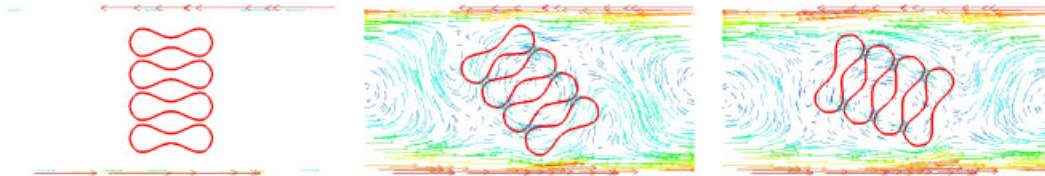
Figure 9. The shear of the four-RBC model at the shear rate of $0.25\,\mathrm{s}^{-1}$ with
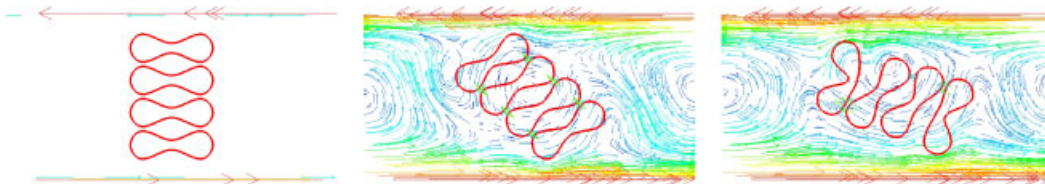cell–cell interaction forces, at $t=0$, 2, and 4 s.

Figure 10. The shear of the four-RBC model at the shear rate of $0.5\,\mathrm{s}^{-1}$ with
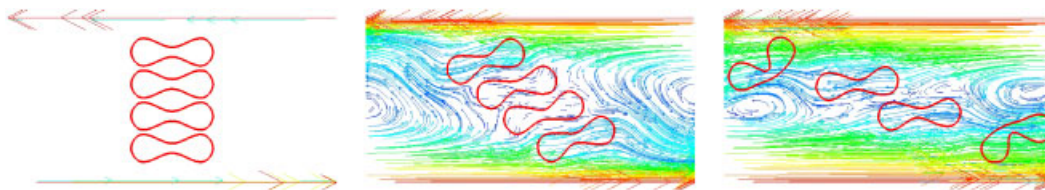cell–cell interaction forces, at $t=0$, 0.5, and 1 s.

Figure 11. The shear of the four-RBC model at the shear rate of $3.0\,\mathrm{s}^{-1}$ with
cell–cell interaction forces, at $t=0$, 0.25, and 0.5 s.

capillaries, large deformations of RBCs cells not only slow down the blood flow, but also enable the exchange of oxygens through capillary vessel walls.

Sickle cell anaemia occurs from genetic abnormalities in haemoglobin which is a complex molecule constituting the most important component of RBCs. When sickle haemoglobin loses oxygen, the deoxygenated molecule form rigid rods which distort the cell membrane into a sickle or crescent shape. The sickle-shaped cells are both rigid and sticky and tend to block capillary vessels and cause the blood flow blockage to the surrounding tissues and organs.

To relate blood rheology to sickle cell anaemia, we consider the normal and sickle RBCs passing through a micro-vessel contraction. The strong viscous shear introduced by such a flow contraction leads to some interesting phenomena of the RBC aggregation with respect to cell–cell interaction forces and cell deformability. Furthermore, the modelling of this complex fluid–solid system also demonstrates the capability of the coupling of the Navier–Stokes equations with protein molecular dynamics.

In this paper, we assign the sickle cell with a crescent shape, higher rigidity and cell–cell adhesive/repulsive forces. Unlike the discrete-particle model presented in References [23, 24], in the proposed method, complex interaction forces between RBCs are modelled with a Morse
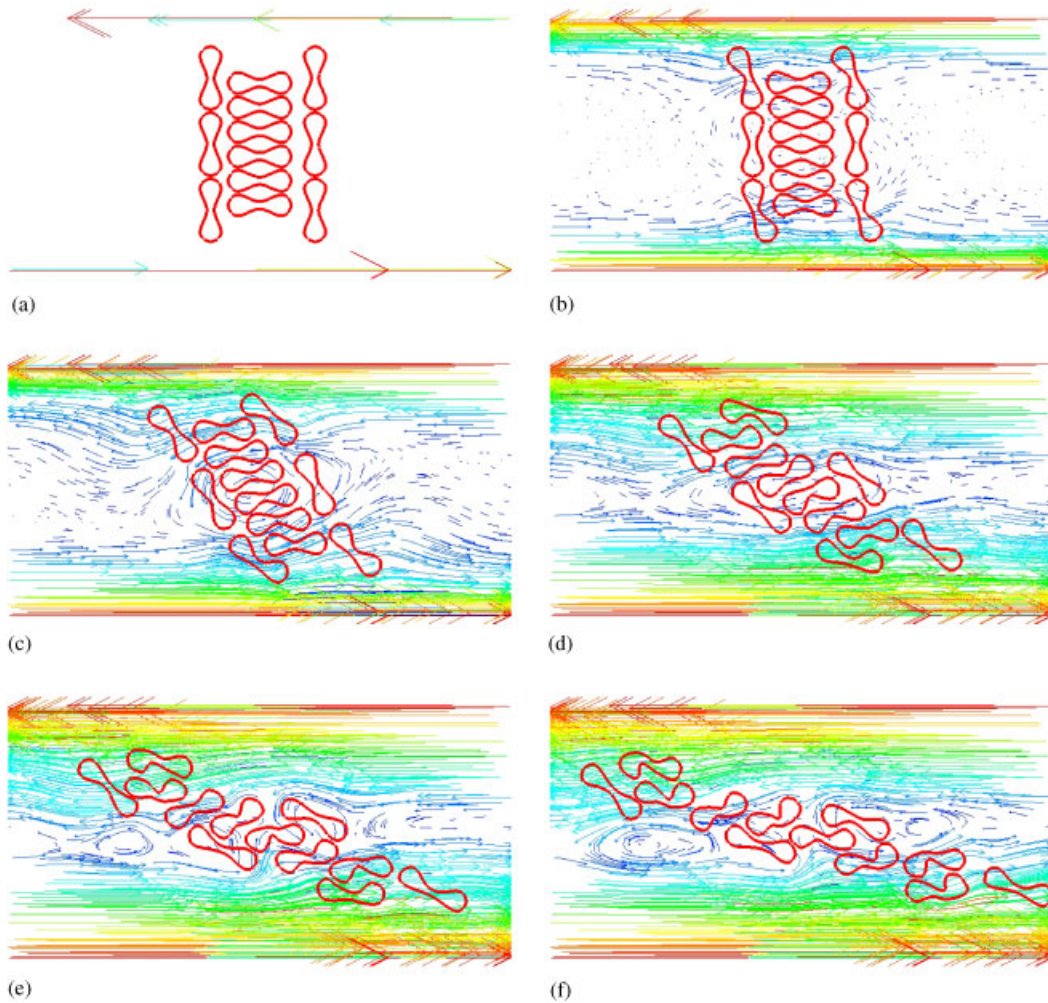
Figure 12. The shear of the twelve-RBC model with the shear rate of 3.0s^{-1}, at
$t = 0\,\text{s}$ (a), $0.6\,\text{s}$ (b), $1.2\,\text{s}$ (c), $1.8\,\text{s}$ (d), $2.4\,\text{s}$ (e), $3\,\text{s}$ (f).

potential and three-dimensional deformable biconcave cells are modelled as individual continuum objects. Thus, we can take advantages of various mature finite element formulations for both fluids and solids.

The initial configurations of the channel and RBCs are depicted in Figure 13. It is shown in Figure 14, as RBCs pass the diffuser stage of the contraction, the deceleration of the RBCs forms blockage for the incoming RBCs. Therefore, dilation of RBCs is coupled with the pile-up of RBCs at the outlet of the vessel constriction.

As also confirmed in Figure 15, under the similar flow conditions, rigid and sticky sickle cells eventually block the micro-vessel entrance which will certainly result in de-oxygenation of surrounding tissues.
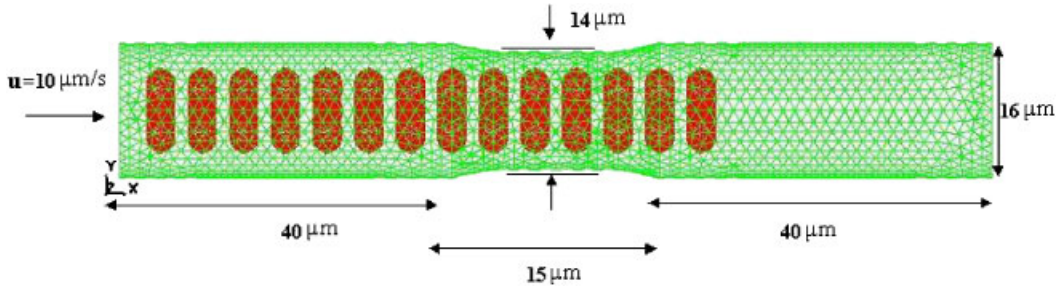
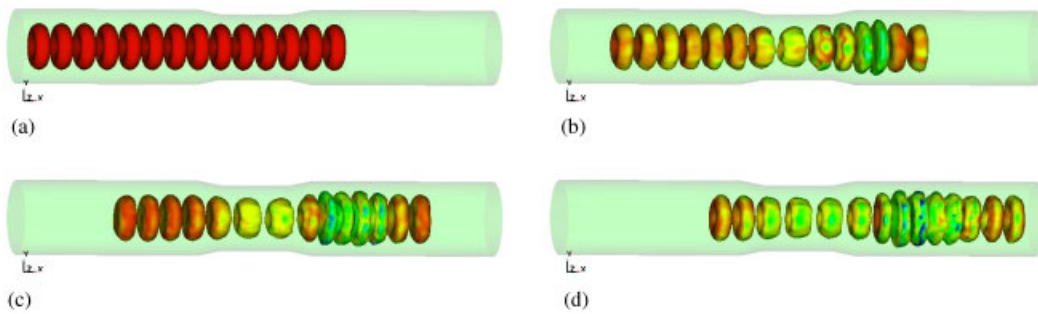Figure 13. The finite element models of RBCs flow passing through a vessel with varying diameters.

Figure 14. The normal RBC cell flow with the inlet velocity of 10 μm/s at
different time steps: (a) $t = 0$; (b) $t = 2$; (c) $t = 4$; (d) $t = 6$.
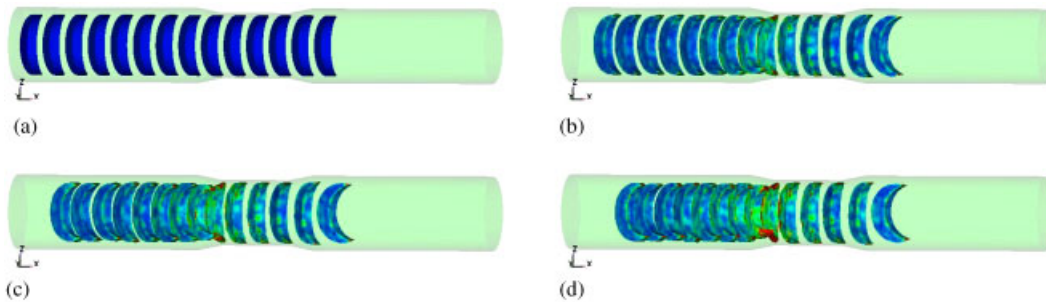

Figure 15. The sickle cell flow with the inlet velocity of 10 μm/s at
different time steps: (a) $t = 0$; (b) $t = 2$; (c) $t = 4$; (d) $t = 6$.

Finally, we present a three-dimensional simulation of a single RBC squeezing through a capillary vessel. The RBC diameter is 1.2 times larger than that of the capillary vessel, which leads to the divergence of the cytoplasm (internal liquid) to the two ends of the capsule by deforming into a slug during the squeezing process. During the exiting process, there is a radial expansion of the slug due to the convergence of the cytoplasm, which deforms the capsule into an acaleph (or jellyfish) shape. In Figure 16, four snapshots illustrate various stages of the RBC with respect to the capillary vessel. The pressure drop within the capillary
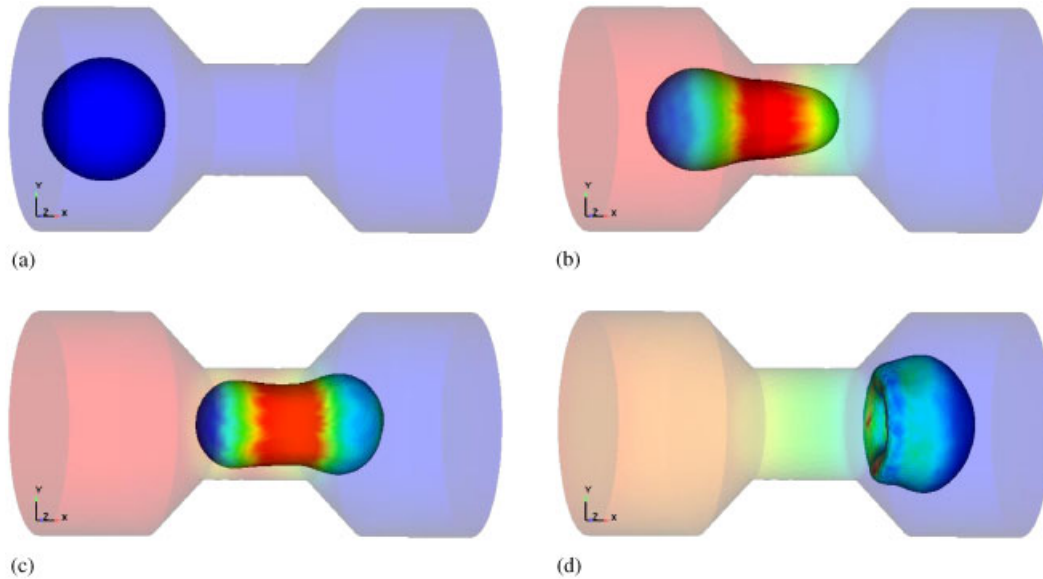
Figure 16. Three-dimensional simulation of a single RBC (essentially a hollow sphere for simplicity) squeezing through a capillary vessel: (a) $t = 0$; (b) $t = 0.48$; (c) $t = 0.96$; (d) $t = 1.44$.
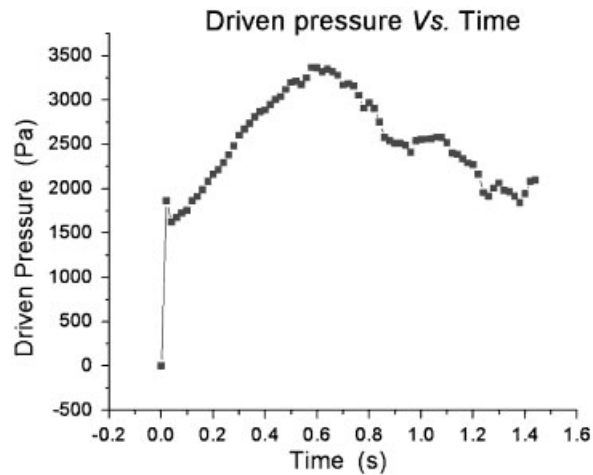

Figure 17. The history of the driven pressure during the squeezing process.

vessel is also presented in Figure 17. The driven pressure here is defined as the average pressure difference between the inlet and outlet of the flow. It is clear that driven pressure level corresponds to the plugged flow which is before the entrance and exit of the deformable cell to the capillary vessel.

5. CONCLUSION

The coupling of the Navier–Stokes equations and protein molecular dynamics in the context of the immersed finite element method provides a unique tool to model complex blood flows within micro- and capillary vessels. In particular, this method models cell–cell adhesive/repulsive forces with special molecular potentials which include the effects of fixed-charge density on the cell membrane, cytoplasm, and protein. This model is applied in several test cases to study the shear-rate-dependent de-aggregation of RBC clusters and the transport of deformable cells (normal and sickle RBCs).

In the near future, using the recent diagnostic medical imaging tools, such as radiopaque dyes and angiograms, physicians will be able to visualize microcirculation flows through the specific regions of the body. The proposed simulation methodology will be an important addition to help understand various physiological phenomena in multi-physics and multi-scale environments.

REFERENCES

1. Huang Y, Doerschuk CM, Kamm RD. Computational modelling of RBC and neutrophil transit through the pulmonary capillaries. *Journal of Applied Physiology* 2001; **90**(2):545–564.
2. Diamond SL. Reaction complexity of flowing human blood. *Biophysical Journal* 2001; **80**:1031–1032.
3. Guo XE, Takai E, Liu K, Wang X. An exploration of cell stress and deformation under shear flow. *Proceedings of ASME IMECE2001 Winter Bioengineering Conference*, BED-23160, New York, NY, 11–16 November 2001.
4. Gao J, Donell B, Deaver DR, Lawrence MB, Dong C. In vitro side-view imaging technique and analysis of human T-leukemic cell adhesion to ICAM-1 in shear flow. *Microvascular Research* 1998; **55**:124–137.
5. Wagner GJ, Moës N, Liu WK, Belytschko TB. The extended finite element method for rigid particles in stokes flow. *International Journal for Numerical Methods in Engineering* 2001; **51**(3):293–313.
6. Wagner GJ, Ghosal S, Liu WK. Particulate flow simulations using lubrication theory solution enrichment. *International Journal for Numerical Methods in Engineering* 2003; **56**(9):1261–1289.
7. Shyy W, Francois M, Udaykumar HS, N'dri N, Tran-Son-Tay R. Moving boundaries in micro-scale biofluid dynamics. *Applied Mechanics Review* 2001; **54**(5):405–453.
8. Wagner GJ. A numerical investigation of particulate channel flow. *Ph.D. Thesis*, Northwestern University, 2145 Sheridan Road, Evanston, IL 60208, June 2001.
9. Zhang L, Gerstenberger A, Wang X, Liu WK. Immersed finite element method. *Computer Methods in Applied Mechanics and Engineering* 2004; **193**(21–22):2051–2067.
10. Evans EA, Fung YC. Improved measurements of the erythrocyte geometry. *Microvascular Research* 1972; **4**:335.
11. Wang X, Liu WK. Extended immersed boundary method using FEM and RKPM. *Computer Methods in Applied Mechanics and Engineering* 2004; **193**(12–14):1305–1321.
12. Zhu C, Bao G, Wang N. Cell mechanics: mechanical response, cell adhesion, and molecular deformation. *Annual Review of Biomedical Engineering* 2000; **2**:189–226.
13. Neu B, Meiselman HJ. Depletion-mediated red blood cell aggregation in polymer solutions. *Biophysical Journal* 2002; **83**:2482–2490.
14. Fung YC. *Biomechanics: Circulation*. Springer: Berlin, 1996.
15. Fung YC. *Biomechanics: Motion, Flow, Stress, and Growth*. Springer: Berlin, 2000.
16. Peskin CS. The immersed boundary method. *Acta Numerica* 2002; **11**:479–517.
17. Chien S. Electrochemical interactions between erythrocyte surfaces. *Thrombosis Research* 1976; **8**:189–202.
18. Tezduyar TE. Stabilized finite element formulations for incompressible-flow computations. *Advances in Applied Mechanics* 1992; **28**:1–44.

19. Hughes TJR, Franca LP, Balestra M. A new finite element formulation for computational fluid dynamics: V. Circumventing the Babuška–Brezzi condition: a stable Petrov–Galerkin formulation of the Stokes problem accommodating equal-order interpolations. *Computer Methods in Applied Mechanics and Engineering* 1986; **59**:85–99.
20. Saad Y, Schultz MH. GMRES: a generalized minimal residual algorithm for solving nonsymmetric linear systems. *SIAM Journal on Scientific and Statistical Computing* 1986; **7**(3):856–869.
21. Zhang L, Wagner GJ, Liu WK. A parallized meshfree method with boundary enrichment for large-scale CFD. *Journal of Computational Physics* 2002; **176**:483–506.
22. Liu WK, Jun S, Zhang YF. Reproducing kernel particle methods. *International Journal for Numerical Methods in Fluids* 1995; **20**:1081–1106.
23. Dzwinel W, Boryczko K, Yuen DA. A discrete-particle model of blood dynamics in capillary vessels. *Journal of Colloid and Interface Science* 2003; **258**(1):163–173.
24. Tanaka H, Araki T. Simulation method of colloidal suspensions with hydrodynamic interactions: fluid particle dynamics. *Physical Review Letters* 2000; **85**(6):1338–1341.